Journal of the Australian Ceramic Society
https://doi.org/10.1007/s41779-022-00796-1

RESEARCH

The effect of alpha-lithium aluminate incorporation on the properties of bovine bone-derived hydroxyapatite

Suleyman Serdar Pazarlioglu[1]

Received: 12 January 2022 / Revised: 10 August 2022 / Accepted: 23 August 2022
© The Author(s) under exclusive licence to Australian Ceramic Society 2022

Abstract

The aim of the present paper was to investigate the effect of alpha-lithium aluminate (α-$LiAlO_2$) incorporation (1, 3, and 5 wt%) on the properties (grain morphology, activation energy for grain growth, decomposition behavior, shrinkage, densification, hardness, fracture toughness, brittleness index, compressive strength, and in vitro bioactivity) of bovine hydroxyapatite (BHA) sintered between 900 and 1300 °C. BHA without α-$LiAlO_2$ incorporation exhibited the shrinkage of 12.02 ± 0.52%, density of 2.86 ± 0.47 g/cm^3, relative density of 90.77 ± 1.51%, porosity of 1.12 ± 0.75%, hardness of 4.19 GPa ± 0.31, fracture toughness of 0.99 ± 0.13 MPam$^{1/2}$, brittleness index of 4.24 ± 0.31 $\mu^{-1/2}$, and compressive strength of 115.75 ± 4.27 MPa, when it was sintered at 1300 °C. It decomposed to beta- and alpha-tricalcium phosphate (β- and α-TCP) as 4.7%, in totally. The activation energy for grain growth of pure BHA was calculated as 77.9 kcal/mol, as 57.61, 59.95, and 71.64 kcal/mol for 1, 3, and 5 wt% α-$LiAlO_2$ incorporated BHAs, respectively. The highest properties for α-$LiAlO_2$ incorporated BHAs were obtained at the sintering temperature of 1200 °C at amount of 5 wt% α-$LiAlO_2$. For this composite, the density of 2.87 g/cm^3, fracture toughness of 1.95 ± 0.18 MPam$^{1/2}$, compressive strength of 218.33 ± 14.02 MPa, and brittleness index of 1.96 ± 0.21 $\mu^{-1/2}$ were obtained. As a result of the in vitro bioactivity test, the bioactivation for this composite became clearly visible in 14 days. The results show that the incorporation of 5 wt% α-$LiAlO_2$ into BHA contributes to increasing the sinterability and properties of BHA without decreasing its bioactivity.

Keywords Bovine hydroxyapatite · Alpha-lithium aluminate · Sintering

Introduction

Development of biomaterials for the repair/replacement of hard tissue has earned much interest in the past few years, although the conventional method of using autogenous or allogenic bone was most preferred for the treatment of bone defects, disadvantages including, the limited quantity and the risk of transmission of infection (e.g., HIV, hepatitis) [1]. Therefore, the development of bone restorative materials with both higher biocompatibility and sufficient mechanical strength is strongly desired. Hydroxyapatite (HA) is one of the most used material in bone regeneration because mainly of its affinity to bone tissues [2]. There are two main ways of producing HA; the first one is inorganic synthesis such as wet-chemical method in aqueous solutions, sol–gel method, hydrothermal method, thermal deposition, continuous precipitation, and solid-state reaction method [3]. The other technique involves extracting HA from natural sources such as meleagris gallopova [4], pig [5], and chicken [6]. It can be also derived from bovine bone [7, 8]. Bovine bone-derived hydroxyapatite (BHA) is currently used in bone grafting for bone repair or replacement and in reconstitution of dental tissues because of its excellent biocompatibility with hard tissues, bioactivity despite its low degradation rate, high osteoconductivity, non-toxicity, non-inflammatory behavior, and non-immunogenic properties [9]. However, the poor mechanical reliability of BHA, due to its high brittleness and poor fracture toughness, restricts its use in load-bearing applications, such as artificial bones or teeth [10]. To improve the mechanical reliability of BHA, incorporation of whiskers, metallic, and/or ceramic materials has been suggested. The incorporation whiskers are not recommended in biomedical applications because of their potential carcinogenicity [11]. There are some papers in literature about

✉ Suleyman Serdar Pazarlioglu
spazarlioglu@marmara.edu.tr

[1] Technology Faculty, Deparment of Metallurgy and Materials Engineering, Marmara University, Recep Tayyip Erdogan Campus, 34854, Maltepe, Istanbul, Turkey

Published online: 12 September 2022

the effect of metallic incorporation materials, such as titanium (Ti) [12], magnesium (Mg) [13], silver (Ag) [14], and stainless steel powders [15] to BHA. However, there are some drawbacks in the incorporation of metallic materials to BHA. First is the need for an inert atmosphere to prevent oxidation of the metallic incorporation material. The second is that metallic incorporation material prevents the homogeneous spread of stresses acting on the BHA implant due to its high modulus of elasticity. Third is the decrease in BHA's ability to bind to bone due to the metals not being bonded to the bone [16]. Fourth is the metallic incorporation materials are not resistant to corrosion over the long term [17]. The properties of BHA, i.e., densification, hardness, compressive strength, and bioactivity, could be succesfully improved by the incorporation of ceramic materials such as cerium oxide (CeO_2) [18], alumina (Al_2O_3) [19], boron oxide (B_2O_3) [20], strontium oxide (SrO) [21], zinc oxide (ZnO) [22], titanium oxide (TiO_2) [23], boron nitride (BN) [24], and mullite [25] without drawbacks explained for whiskers and/or metallic materials. However; there is limited paper in the literature about the effect of lithium containing incorporation material on the properties of BHA. Celik, H. H. et al. [26] have used Li_2CO_3 as incorporation material to BHA and investigated the effect of sintering temperature and Li_2CO_3 ratio on the properties of BHA by artificial neural networks. Shainberg, A. P. M. et al. [27] have investigated the biocompatibility and bioactivity properties of BHA modified through Li_2CO_3 (0.25–2 wt%). They suggest that BHA-0.25 wt% Li_2CO_3, sintered at 1300 °C, combines the necessary physical and structural qualities with favorable biocompatibility characteristics. In the light of literature survey, no study was found on the effect of α-lithium aluminate (α-$LiAlO_2$), which is one of the lithium containing material, incorporation to the properties of BHA.

In the Li_2O-Al_2O_3 system, at least five compounds with different stoichiometric Li/Al ratios are identified including Li_5AlO_4, Li_3AlO_3, $LiAlO_2$, $Li_2Al_4O_7$, and $LiAl_5O_8$ [28]. $LiAlO_2$ has three allotropes: first, α-$LiAlO_2$, the low temperature (400 °C) form; second, β-$LiAlO_2$, the intermediate temperature (400–800 °C) form; and third, γ-$LiAlO_2$ which is the most stable form at high temperature (≥ 900 °C) [29]. α-$LiAlO_2$ has a hexagonal structure where the cations have octahedral coordination. In this structure, each lithium and aluminum ion is surrounded by six oxygen ions. β-$LiAlO_2$ has an orthorhombic crystal structure and the aluminum ions have both tetrahedral and octahedral coordination with the oxygen ions. Tetrahedral coordination has each lithium and aluminum ion surrounded by four oxygen ions. γ-$LiAlO_2$ is $P4_12_12$ with a tetragonal crystal structure with cell dimensions $a = 5.1687$°A and $c = 6.2697$°A, and with each cation tetrahedrally coordinated with the oxygen ions [30, 31]. $LiAlO_2$ is one of the compounds in the applications of optically stimulated luminescence (OSL) dosimetry [32] tritium breeder of a nuclear fusion reactor, molten carbonate fuel cells, coating of electrodes to improve the electrochemical performance of lithium ion batteries [33], and lithium secondary battery [34]. $LiAlO_2$ having a low effective atomic number (~7.6) and is nearly equal to human tissue (~7.2) [35]; however, no paper was found regarding its usability in the human body as in bulk form and/or incorporation material to BHA.

This study presents the effect of α-$LiAlO_2$ on the properties of BHA. For this purpose, BHA with and without α-$LiAlO_2$ incorporations were subjected to sintering and characterized using different techniques.

Experimental procedure

Sample preparation

BHA powders were derived from bovine bones by the following steps: bovine femur bones (2–4 years) were cleaned to remove visible tissues and substances on the surface of bones. Marrows in all of the bones were removed via boiling within water in a pressure cooker for 4 h. After the boiling process, the retained shafts were deproteinized with sodium hydroxide (NaOH) for 1 h, washed with distilled water, and then calcinated at 800 °C with a heating rates of 5 °C/min for 4 h to ensure that the organics are completely removed to eliminate any microbial contaminations. The calcinated bones were ground and then crushed in a mortar to produce BHA powders between − 63 to + 45 µm. α-$LiAlO_2$ powder (99.5% in purity; Sigma Aldrich, USA) (separately) with 1, 3, and 5 wt.% was added to BHA and the prepared mixtures were homogenized 4 h with 200 r/min rotating speed for using a ball milling device in a zirconia-coated stainless steel jar with the addition of ethyl alcohol and zirconia balls in order to produce composites. The mixed powders were dried in an oven at 105 °C for 1 day, and then, both BHA and the composite powders at a weight of 2.0 g were pelleted using uniaxial press at 350 MPa to obtain the samples, as in our previous study [36]. Before sintering treatments, the green bodies were dried at 105 °C for 1 day. The compacted samples were sintered in air condition at temperatures ranging from 900 to 1300 °C, at furnace ramp rate of 5 °C, and soaking time of 4 h and then cooled to room temperature ramp rate of 5 °C at air atmosphere.

Determination of physical and mechanical properties

In order to determine the physical and mechanical properties of BHA with and without α-$LiAlO_2$ incroporation, shrinkage, density, porosity, relative density, hardness, fracture toughness, brittleness index, and compressive strength

examinations were performed. Calculation of shrinkage (%) ratios was carried out by comparison of the thickness of each sample before and after the sintering process with an electronic caliper which has 1/1000 sensitivity as shown in Eq. (2.1).

$$S = \left(\frac{L_0 - L_1}{L_0}\right) x100 \tag{2.1}$$

Here, S is the shrinkage (%), L_0 is the thickness before sintering (mm), and L_1 is the thickness after sintering (mm).

Sintered density (ρ), porosity (p), and theoretical density (ρ_t) of the samples were calculated using Eqs. (2.2), (2.3), and (2.4), respectively. The relative density (ρ_r) values were determined by Eq. (2.5):

$$\rho = \frac{M_k}{M_a - M_s} \tag{2.2}$$

$$p = \left(\frac{M_a - M_k}{M_a - M_s}\right) \times 100 \tag{2.3}$$

Here, ρ is the density (g/cm^3), p is the porosity (%), M_k is the dry weight, M_a is the wet weight of the sample, and M_s is the wet weight of the suspension in distilled water.

$$\rho t = \frac{m_t}{(\frac{m_1}{d_1} + \frac{m_2}{d_2})} \tag{2.4}$$

$$\rho_r = \frac{\rho}{\rho_t} \tag{2.5}$$

Here, ρ_t is the theoretical density, ρ_r is the relative density, m_t is the total weight of the mixture (g), m_1 is the weight of BHA in the mixture (g), d_1 is the theoretical density of BHA (3.156 g/cm^3 [37]), m_2 is the weight of α-$LiAlO_2$ in the mixture (g), and d_2 is the theoretical density of α-$LiAlO_2$ (3.403 g/cm^3 [38]).

Before hardness and fracture toughness measurements, the samples were firstly ground with 800, 1200, 2500, 4000, and 5000 mesh SiC paper and then polished with 10, 5, 3, and 1 µm diamond paste to obtain mirror-like surfaces. Hardness and fracture toughness measurements were performed by Future Tech FM 301 microhardness device at loads of 200 and 300 g for 20 and 10 s, respectively. The average and standard deviation values obtained to both tests were taken from 10 indents. They were calculated by Eqs. (2.6) and (2.7), respectively. The brittleness index (B) was determined by Eq. (2.8) [39].

$$HV = 0.0001854\frac{F}{d^2} \tag{2.6}$$

Here, HV is the hardness (GPa), F is the applied force (N), and d is the average indentation diameter (mm).

$$K_{\pi c} = 0.203(\frac{c}{a})^{-1.5} HVa^{0.5} \tag{2.7}$$

Here, K_{IC} is the fracture toughness, c is the radial crack dimension measured from the centre of the indent impression (m), and a is the half diagonal of the indentation (m).

$$B = \frac{H}{K_{\pi c}} \tag{2.8}$$

Compression tests were carried out on 10 samples using a universal testing machine (Devotrans FU 50kN, Turkey) under a loading rate of 2 mm min^{-1}.

Characterization

Phase analysis was performed to the powders obtained from compression test samples crushed by using agate mortar. XRD analyses were conducted by a Philips X'Pert X-ray diffraction machine at room temperature using Cu-Kα as the radiation source at a scan speed of 0.6° per minute and a step scan of 0.02° in the range of 2θ values between 20° and 60°. The percentage of the phases detected by XRD analysis was determined by Rietveld analysis. The changes in the surface morphology of the sintered samples were determined by FEI Sirion XL30 SEM machine. The changes in the average grain size of the sintered samples were determined by the linear intercept method, and the activation energy for grain growth on the surface-sintered samples was calculated using Eq. (2.9).

$$D = A\ exp\left[-\frac{Q}{RT}\right] \tag{2.9}$$

Here, D is the average grain size, T is the temperature, and R is the gas constant, i.e., 8.314 kJ/kmol K.

Evaluation of in vitro bioactivity

The specimens having the high mechanical properties were prepared in a disk shape with the dimensions of 11 × 4 mm^2 (diameter × thickness) after sanding up to 1200 mesh SiC paper and sterilization (autoclaving, 120 °C, 20 min) for in vitro tests. The evaluation of in vitro bioactivity was carried out by soaking the pellets mounted vertically, in 40-mL simulated body fluid (SBF) prepared according to ref [40] at pH 7.32 and maintained at 37 ± 1 °C for 7, 14, and 28 days. The 40-mL SBF solutions used in the in vitro tests were changed every day. At a specified time, the samples were taken from the SBF solutions without damaging the apatite layers and cleaned using distilled water. Finally, the samples were dried at 60 °C for 12 h. The apatite layers on the

surface of samples immersed in SBF solutions were investigated by SEM.

Results and discussion

Figure 1 shows the XRD patterns of BHA without α-$LiAlO_2$ incorporations. It only consisted of HA peaks up to temperature of 1100 °C. However, it began to decompose into beta-tricalcium phosphate (β-TCP) and alpha-tricalcium phosphate (α-TCP) phases at the temperatures of ≥ 1100 °C. The same regime has been confirmed by ref [41]. At these temperatures, the β-TCP ratios were measured as 3.3%, 3.4%, and 3.9%, and the α-TCP ratio was measured as 0%, 0.3%, and 0.8%, respectively. In the light of literature survey, only one paper was found on the investigation of thermal stability of BHA by Rietveld analysis [42]. In that paper, no decomposition was reported for hydrothermally derived BHA, which had sintered at 1200, 1400, and 1500 °C. The highest decomposition ratio of BHA in the present paper was obtained at 1300 °C as 4.7%, in totally. But, it has an appropriate decomposition ratio for use in the human body according to ISO 13779–3:2018 standart [43].

Figure 2 shows the XRD patterns of α-$LiAlO_2$ incorporated BHAs. In these samples, the phases of HA, γ-$LiAlO_2$, calcium aluminates ($CaAl_4O_7$, $Ca_4Al_6O_{13}$, and $Ca_9Al_6O_{18}$), and hilgenstockite were detected. As explained in the introduction section, the presence of γ-$LiAlO_2$ phase in the composites is due to the allotropic transformation of $LiAlO_2$ and high thermal stability of γ-$LiAlO_2$ at ≥ 900 °C. The term of calcium aluminate is used for a series of compounds with different Ca/Al ratios [44]. In the CaO-Al_2O_3 system, there are nine types of calcium aluminates: $CaAl_2O_4$, $CaAl_{12}O_{19}$, Ca_3AlO_6, $Ca_3Al_2O_6$, $Ca_5Al_6O_{14}$, $Ca_{12}Al_{14}O_{33}$, $CaAl_4O_7$, $Ca_4Al_6O_{13}$, and $Ca_9Al_6O_{18}$ [45, 46]. As stated by ref [47] in Li_2O-CaO-Al_2O_3 system, calcium aluminates of $CaAl_2O_4$, $CaAl_{12}O_{19}$, and $Ca_3Al_2O_6$ occurs between 1370 and 1420 °C. Previous study on HA-Al_2O_3 composite [48] show that the presence of $CaAl_2O_4$ accelerates the decomposition of HA and reduces the decomposition temperature to 1150 °C. $CaAl_4O_7$ has a monoclinic structure of the type C2/c, and its lattice parameters are $a = 1.289$ nm, $b = 0.889$ nm, $c = 0.544$ nm, and $\beta = 106.938$ [49]. The reactive groups on the surface of $CaAl_4O_7$ supports the easy attachment of organic acids to the first step in the covalent linkage system for antibiotics [50]. The $Ca_4Al_6O_{13}$ phase occurs at 900 °C [51] and has an orthorhombic crystal lattice structure with the lattice parameters of $a = 5.300$ Å, $b = 17.761$ Å, and $c = 21.088$ Å [52]. As stated by ref [53] that $\alpha \rightarrow \gamma$-$LiAlO_2$ transformation starts at 850 °C, and during the $\alpha \rightarrow \gamma$-$LiAlO_2$ transformation, the Al-O and Li–O distances in the α-$LiAlO_2$, equal 1.92 and 2.08A°, respectively, get shorter to 1.76 and 2.06 A° in the γ-phase lattice. Calcium aluminate phases detected in the present study were formed due to the following reasons: first is the decreasing in the Al-O distance during the transformation of α to γ-$LiAlO_2$. Second is the diffusion of Ca^{2+} in BHA, which has the ion radii of 1.00A° [54], into Al-O gap when the temperature for the

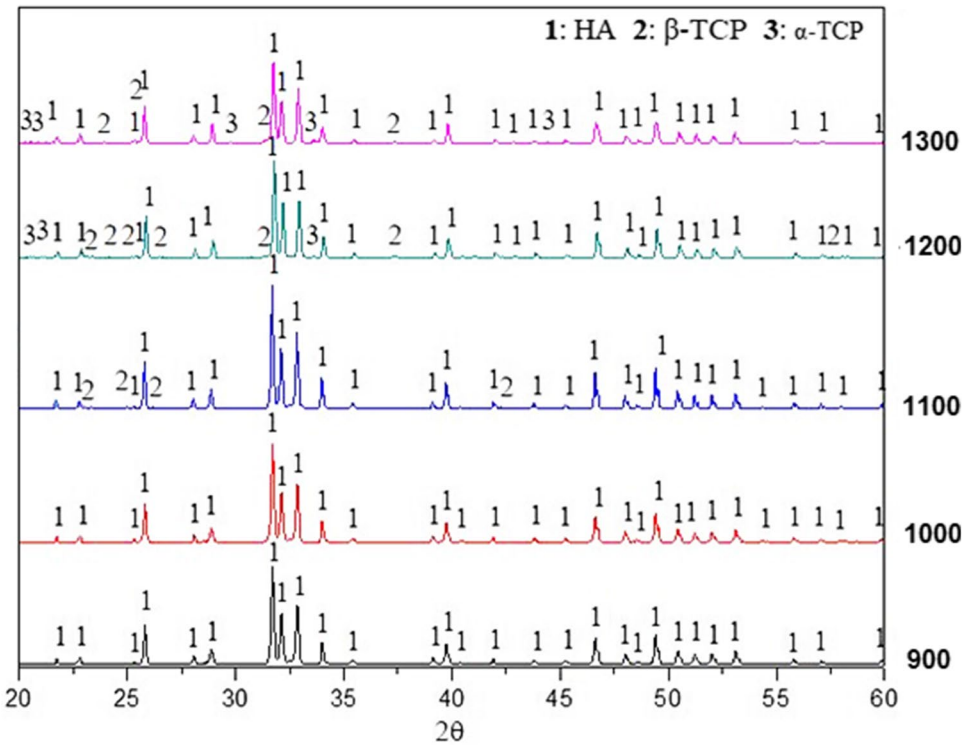


Fig. 1 XRD patterns of BHA without α-$LiAlO_2$ incorporations

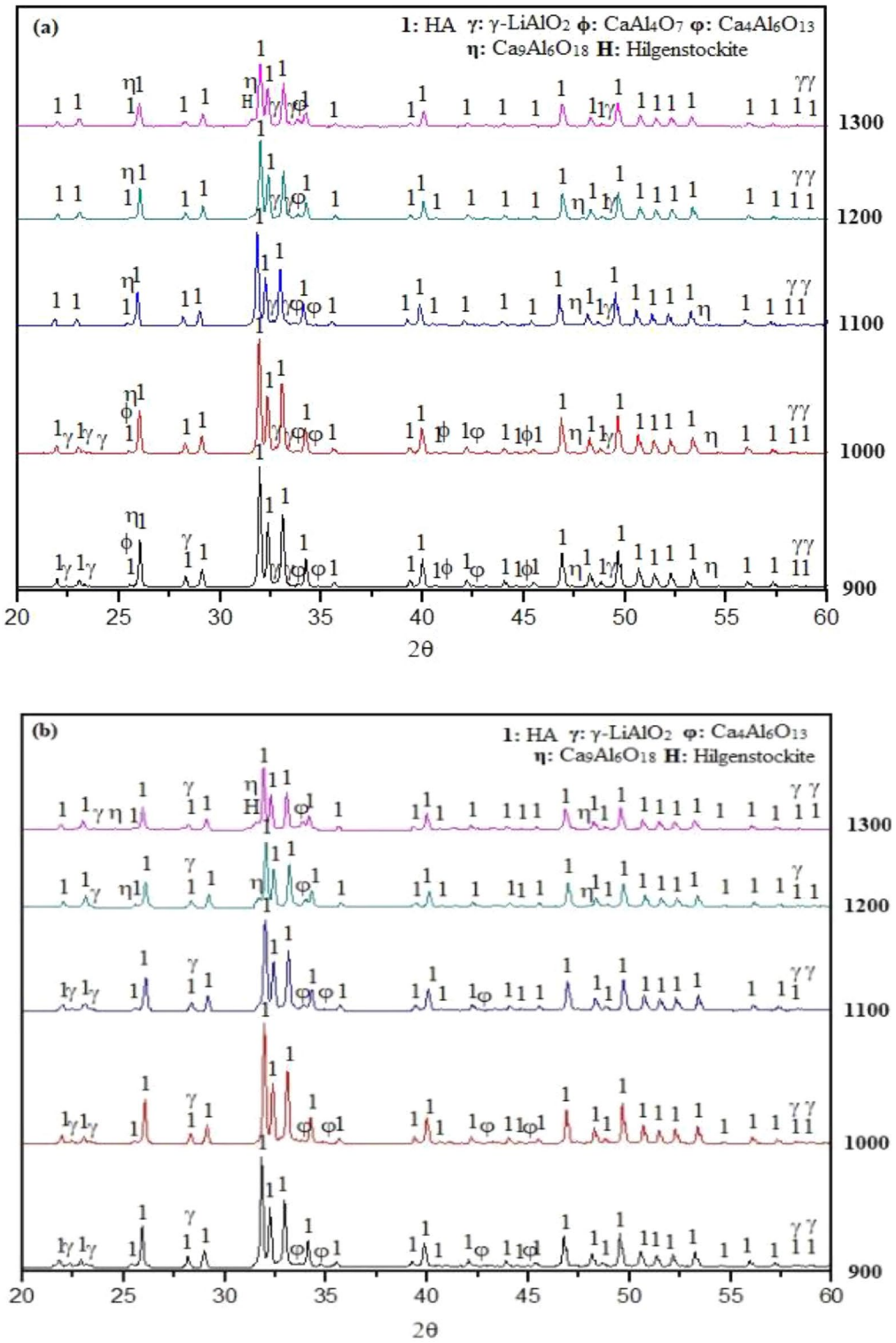


Fig. 2 XRD patterns of **a** 1 wt% α-$LiAlO_2$, **b** 3 wt% α-$LiAlO_2$, and **c** 5 wt% α-$LiAlO_2$ incorporated BHAs

transformation of α to γ-$LiAlO_2$ is reached. Third is due to the enthalpy values required for the formation of $CaAl_4O_7$, $Ca_4Al_6O_{13}$, and Ca_9Al_6O18 are much lower than the others, as calculated by ref [55]. Hilgenstockite detected in α-$LiAlO_2$ incorporated BHAs is also known as tetracalcium phosphate (TTCP) and crystallizes in the monoclinic unit cell in space group P21with unit cell parameters $a = 7.023$ Å, $b = 11.986$ Å, $c = 9.473(2)$ Å, and $b = 90.90°$ [56]. It is used

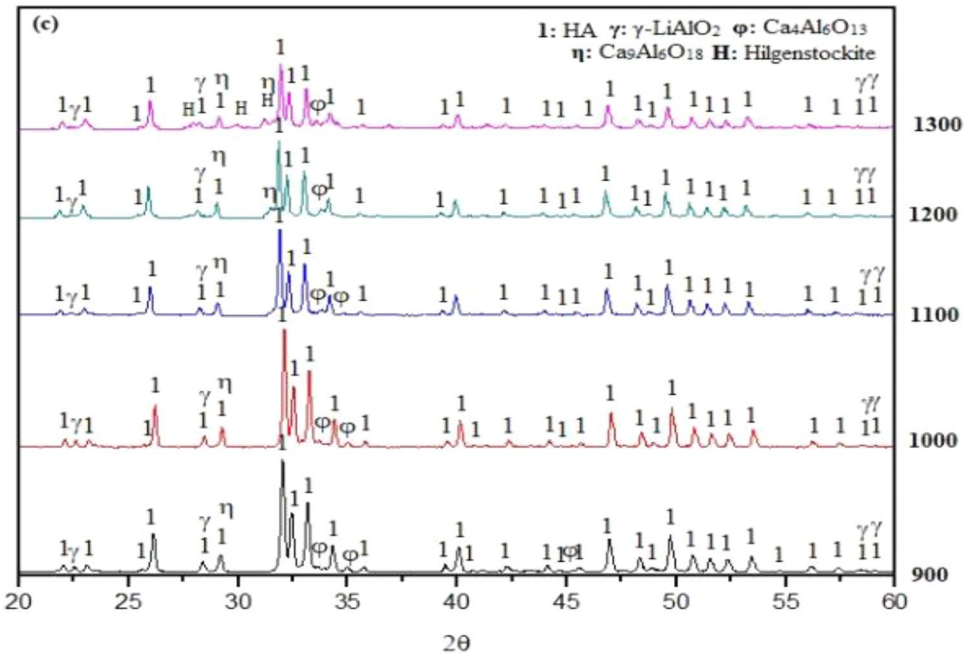


Fig. 2 (continued)

in the medical and pharmacy applications such as bone and dental cement and drugs because of its particular material characteristic, which has good biocompatibility, bioresorbable, biomimetic, and good osteoconductivity [57]. The presence of hilgenstockite means that α-$LiAlO_2$ incorporated BHAs sintered at 1300 °C decomposed to TTCP without the formation of β- and/or α-TCP phases. However, in a previous study about BHA-bioglass composite, a decomposition at about 61% was observed in BHA to $\beta+\alpha$-TCP after sintering at 1300 °C [58]. The presence of TTCP without calculation of its amount by Rietveld analysis at the sintering temperature of 1300 °C has also confirmed by a previous study, which is about the BHA-$CaTiO_3$ composites [59]. The rate of TTCP depending on the increasing α-$LiAlO_2$ incorporation in the BHA were calculated as 0.2%, 0.5%, and 1.2%, respectively. However, it was declared in a previous study [60], the incorporation of 5 wt% Al_2O_3 caused to decrease in the decomposition temperature of synthetic HA from 1100 to 900 °C, and increase the decomposition rate up to 31.8% at 1300 °C. It means that the incorporation of α-$LiAlO_2$ instead of Al_2O_3 can increase the stabilization of BHA.

SEM micrographs of pure BHA and the composites are shown in Fig. 3 and Fig. 4, respectively. It has been revealed from SEM images that a huge amount of pores do exists among the grains up to sintering temperature of 1100 °C because of the pure sinterability. Up to this temperature, the average grain size of the samples increased from 0.37 to 0.83 μ with increasing temperature and α-$LiAlO_2$ ratio (Fig. 5). Although pure BHA has a higher porous surface morphology at 1200 °C sintering temperature, α-$LiAlO_2$ incorporated BHAs have become composed of uniform, and small grains with the increase of α-$LiAlO_2$ incorporation. The average grain size of 1.50 μ of pure BHA at this temperature decreased to 1 μ with a 50% decrease with increasing in α-$LiAlO_2$ incorporation. At 1300 °C, at about 30%, reduction was achieved in the 2.98-μ grain size of pure BHA with the incorporation of 1 wt% α-$LiAlO_2$. At this temperature, microcracking as indicated by the white arrows was observed in the grains and/or near the grain boundaries of pure BHA, 3 wt%, and 5 wt% α-$LiAlO_2$ incorporated BHAs. In a previous study, microcracking was also observed to the bioglass added BHA, when sintering carried out at 1220 °C [61]. Tough and strong ceramics are produced with sintering process. “Sintering” is the term used to describe the consolidation of the product during firing. Consolidation implies that, within the product, particles have joined together into strong aggregate. The term sintering is often interpreted to imply that shrinkage and densification have occurred. Sintered HA implants are observed to develop microcracks [62]. Microcracking in HA ceramic materials occurs because of the two main reasons: first is the thermal expansion anisotropy of HA [63], which leads to the generation of thermal and residual stress fields as well as it results in contraction of individual grains from neighboring grains at different rates when the pure HA ceramics sintered using the conventional sintering process [64]. Such a microcracking can be eliminated if the average grain size of the sintered HAp is less than the critical grain size. It had calculated as

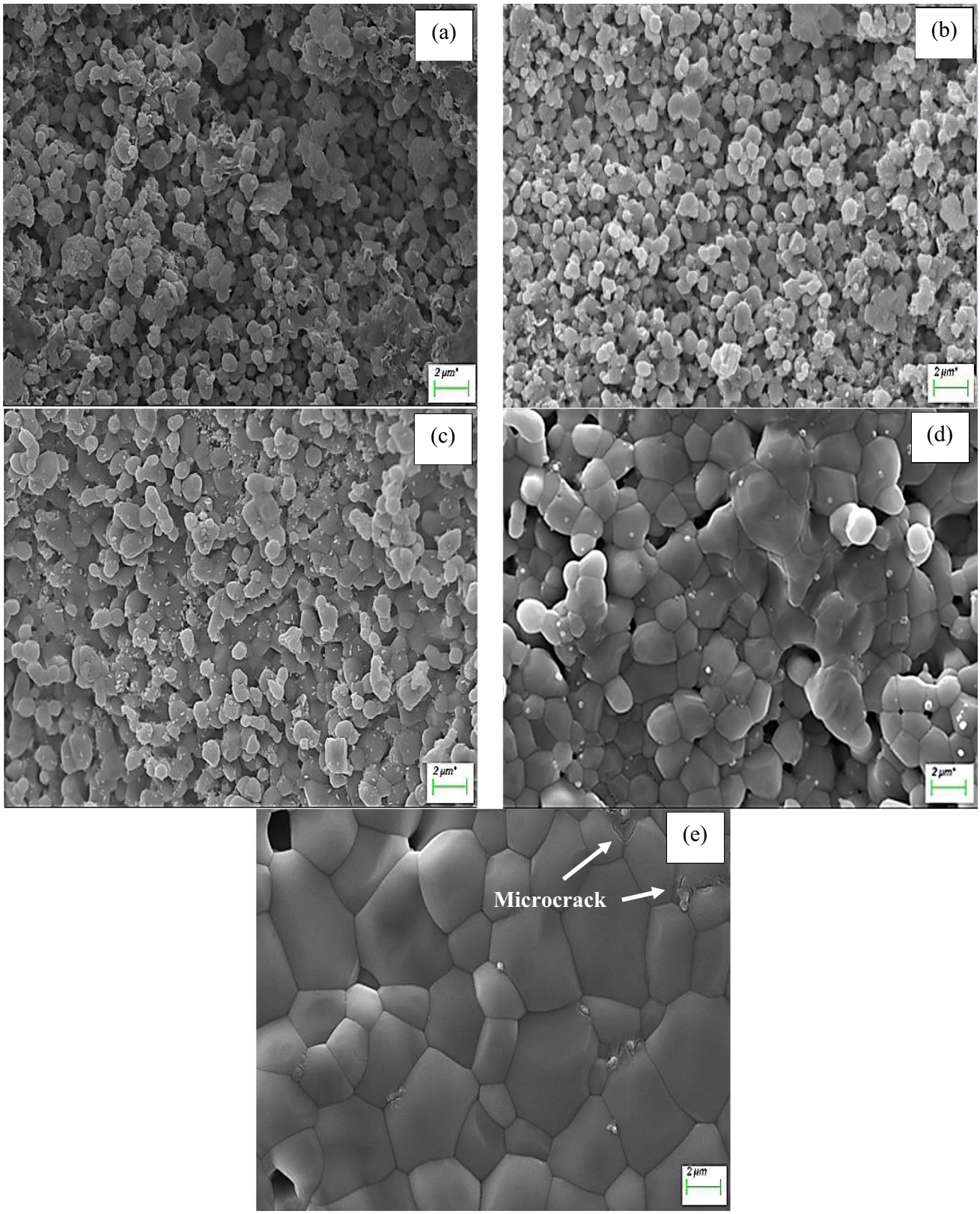


Fig. 3 SEM images of pure BHA sintered at **a** 900 °C, **b** 1000 °C, **c** 1100 °C, **d** 1200 °C, and **e** 1300 °C

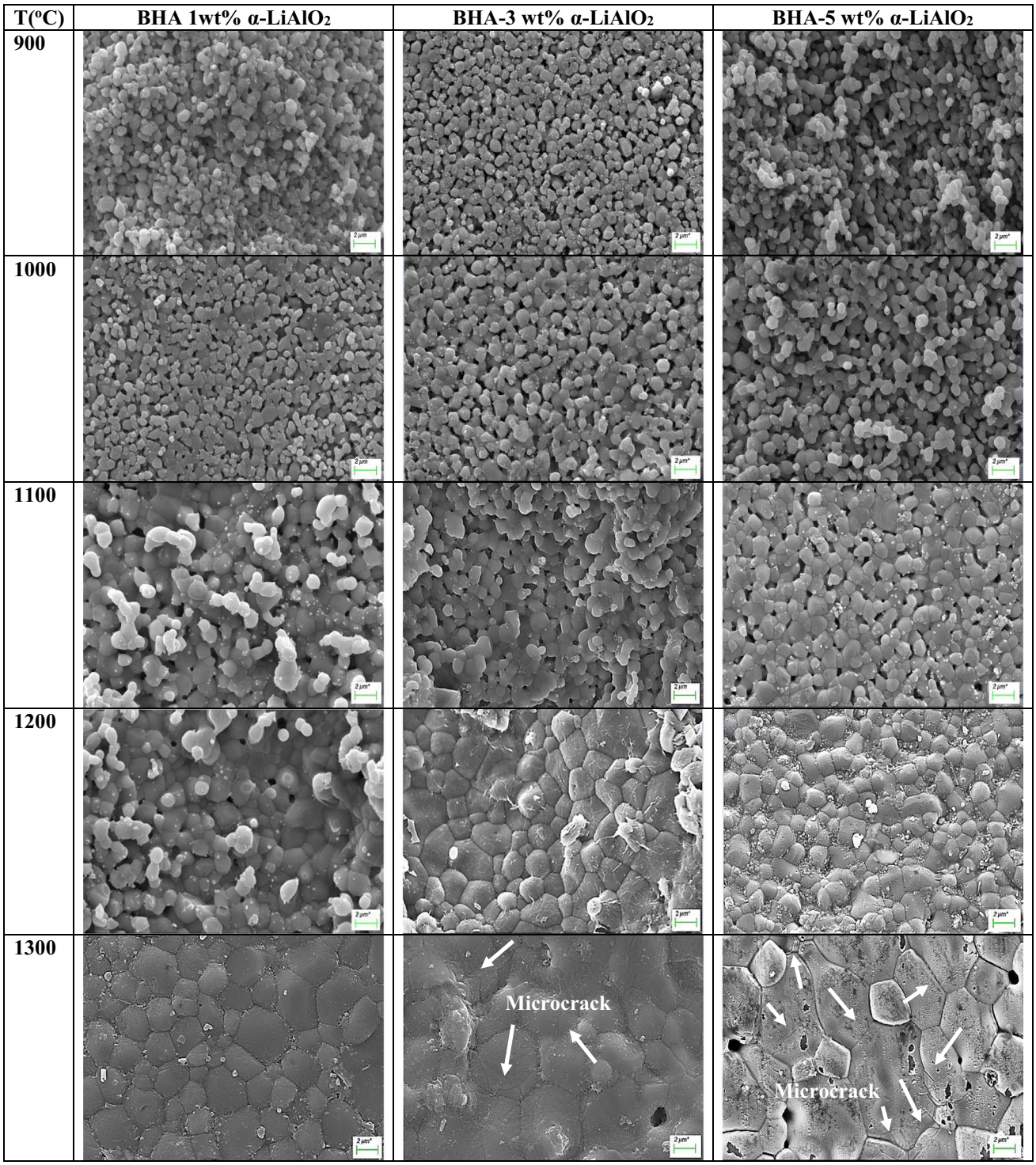


Fig. 4 SEM images of α-$LiAlO_2$ incorporated BHAs

0.4 μ for hot-pressed HA [65], 1.1 μ for synthetic HA [66], and 2.72 μ for synthetic HA-10 wt% ZrO_2 composite [67]. In the present study, the critical size for the elimination microcracking is 1.5–2.3 μ for pure BHA and 1.97 μ for α-$LiAlO_2$ incorporated BHAs. Second is the difference coefficient of thermal expansion between secondary phases (β- and α-TCP, and TTCP) and HA leads to microcracking in HA ceramics [68]. The incorporation of α-$LiAlO_2$ at amount 5 wt% led to increase in grain size of pure BHA from 2.98 to 3.51 μ (at about 17%), and the more microcracking than did 3 wt%

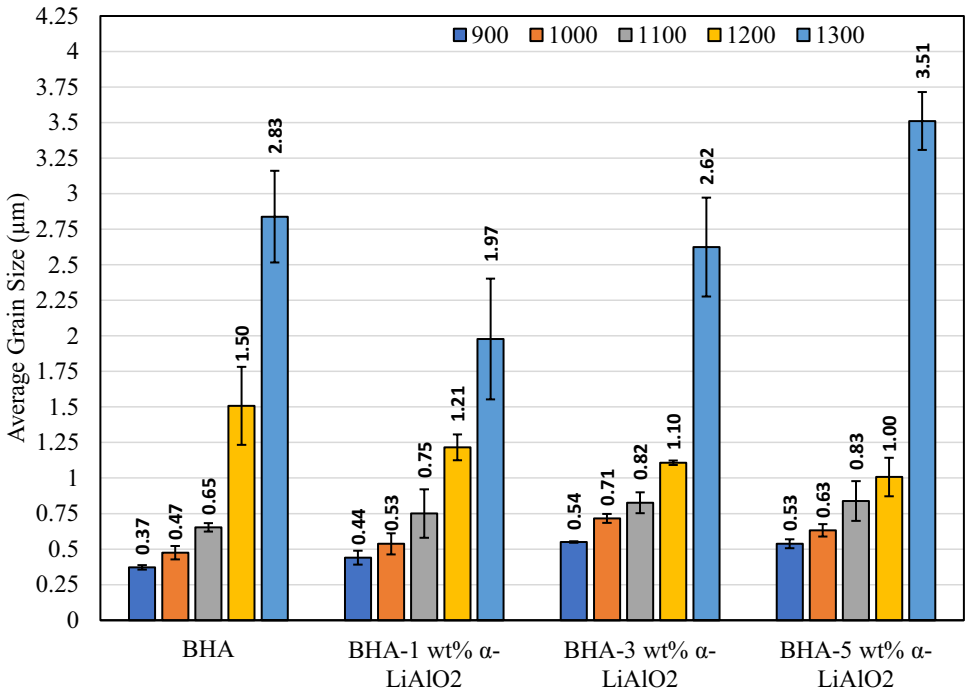


Fig. 5 Average grain sizes of BHA with and without α-$LiAlO_2$ incorporations

α-$LiAlO_2$ incorporation, when sintering was carried out at 1300 °C. However; the microcrack intensity, the average grain size, and increment in grain size of 5 wt% α-$LiAlO_2$ incorporated BHA were lower than the HAs that were sintered at 1300 °C and incorporated with various oxide ceramics such as ZrO_2 [69] and TiO_2 [70].

Figure 6 shows the activation energies were calculated from the Arrhenius plots as function of the sintering temperature for BHA and composites. It was calculated as 77.91 kcal/mol for pure BHA and as 57.61, 59.95, and 71.64 kcal/mol for 1, 3, and 5 wt% α-$LiAlO_2$ incorporated BHAs, respectively. The activation energy value of pure

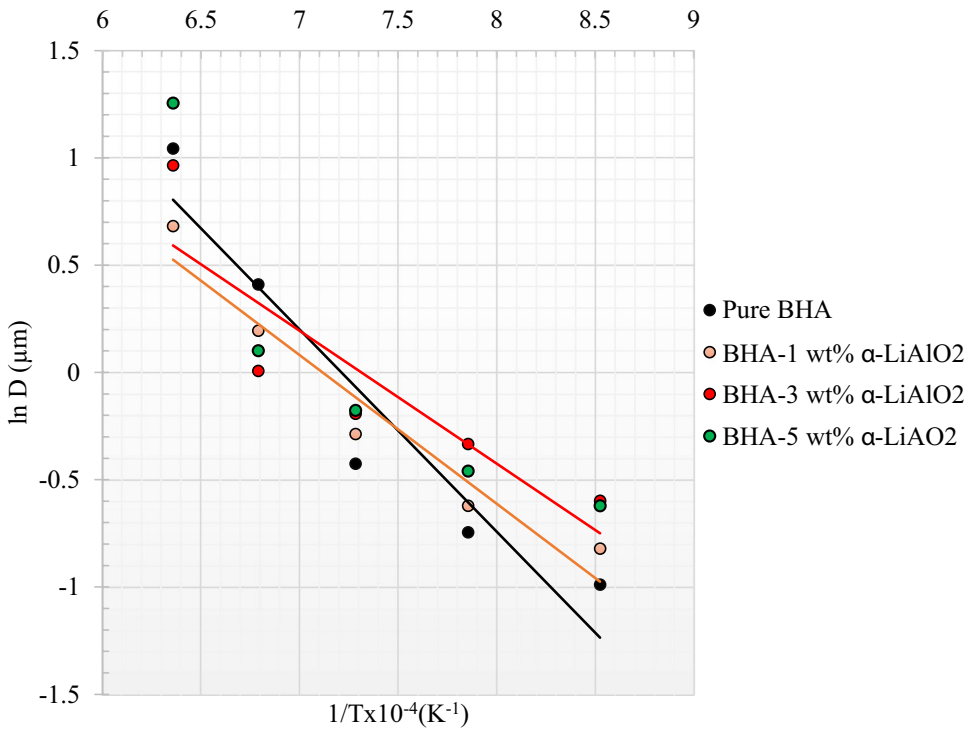


Fig. 6 Activation energy curves of BHA and composites

BHA is in good agreement with the values reported by other researchers, e.g., 77.78 kcal/mol [71] and 84.1 kcal/mol [72]. Since lower activation energies for grain growth were observed for the α-$LiAlO_2$ incorporated BHAs, as compared to pure BHA, it can be considered that the phases in α-$LiAlO_2$ incorporated BHAs increased the mass transport during the sintering process, allowing for high densification to be achieved without abnormal grain growth.

Figures 7 and 8 show the physical and mechanical properties of BHA and α-$LiAlO_2$ incorporated BHAs depending on the sintering temperature. In the case of sintering at low temperatures, i.e., between 900 and 1100 °C, poor properties in physically and mechanically were observed due to the fact that the sintered samples had a relatively high open porosity. Figure 7a shows the shrinkage in thickness of sintered bodies. The highest shrinkage in thickness for pure BHA was calculated as $12.02 \pm 0.52\%$ at 1300 °C. Previous studies have reported that the maximum shrinkage in thickness for BHA is 10.2% pelleted at 150 MPa [73], 10.81% pelleted at 200 MPa [74] after sintering at 1300 °C. This means that the highest shrinkage in thickness occurs for BHA powders at the high uniaxial pressure due to the decrease in the distance between the BHA powders in the green bodies and sintering contributes to high shrinkage during grain formation. The highest shrinkage in thickness was calculated as $11.51 \pm 0.49\%$ for 1 wt% α-$LiAlO_2$ incorporated BHA at same temperature. However, the highest values of shrinkage in thickness of $11.66 \pm 0.52\%$ and $11.68 \pm 0.44\%$ were calculated at 1200 °C for 3 wt% and 5 wt% α-$LiAlO_2$ incorporated BHAs, respectively. Sintering at 1300 °C led to decreasing in the shrinkage in thickness of α-$LiAlO_2$ incorporated BHAs from 11.51 ± 0.49 to $9.85 \pm 0.63\%$ with the increasing in α-$LiAlO_2$ incorporation ratio. The same regime was also observed to other physical and mechanical properties of 3 wt% and 5 wt% α-$LiAlO_2$ incorporated BHAs. For example, the density decreased from 2.832 ± 0.003 to 2.682 ± 0.015 g/cm^3, the relative density decreased from 89.94 ± 0.12 to $85.85 \pm 0.50\%$, the hardness decreased from 3.05 ± 0.86 to 2.08 ± 0.65 GPa, the fracture toughness decreased from 1.46 ± 0.30 to 1.24 ± 0.28 MPam$^{1/2}$, the

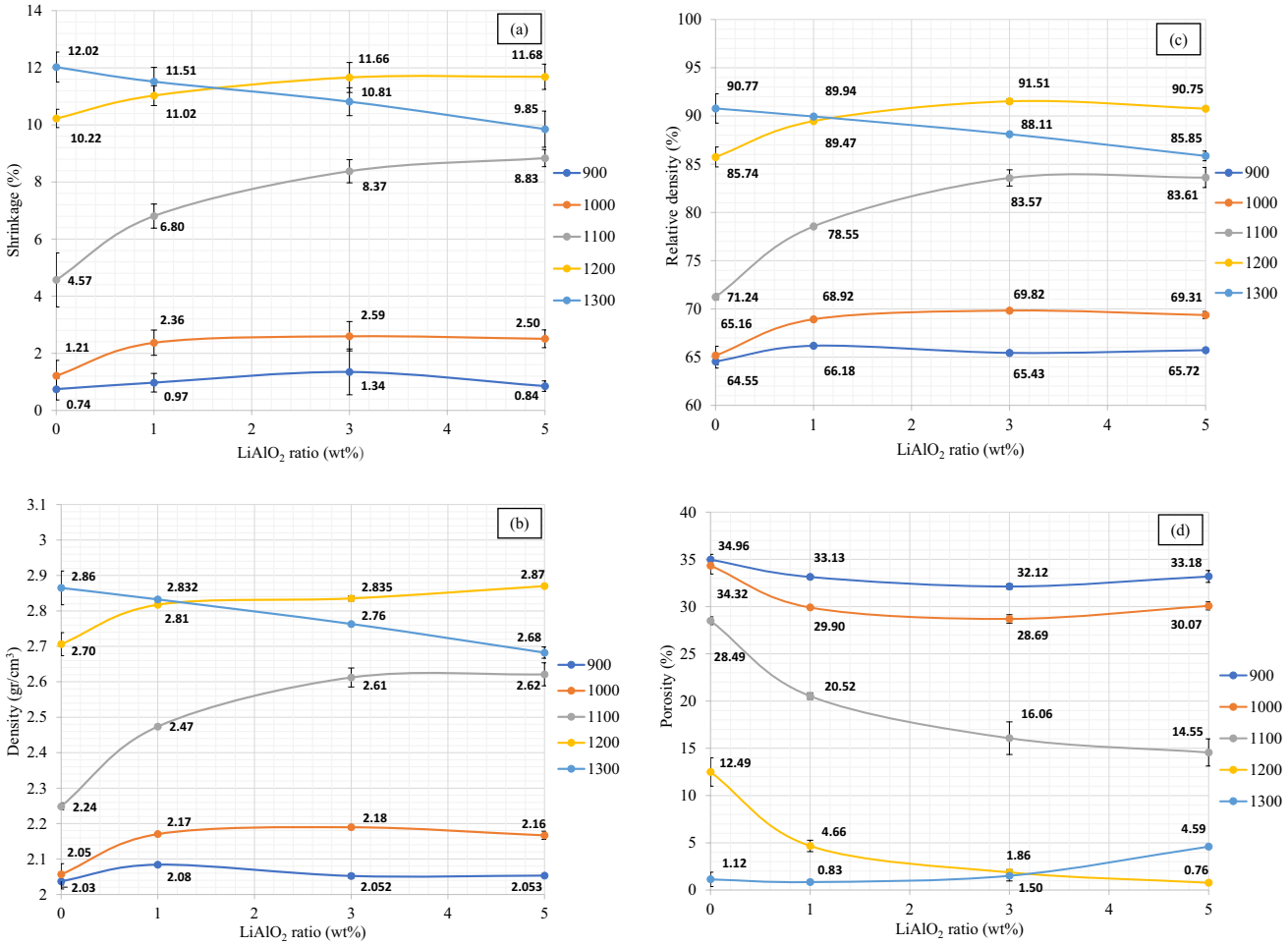


Fig. 7 Physical properties of pure BHA and α-$LiAlO_2$ incorporated BHAs

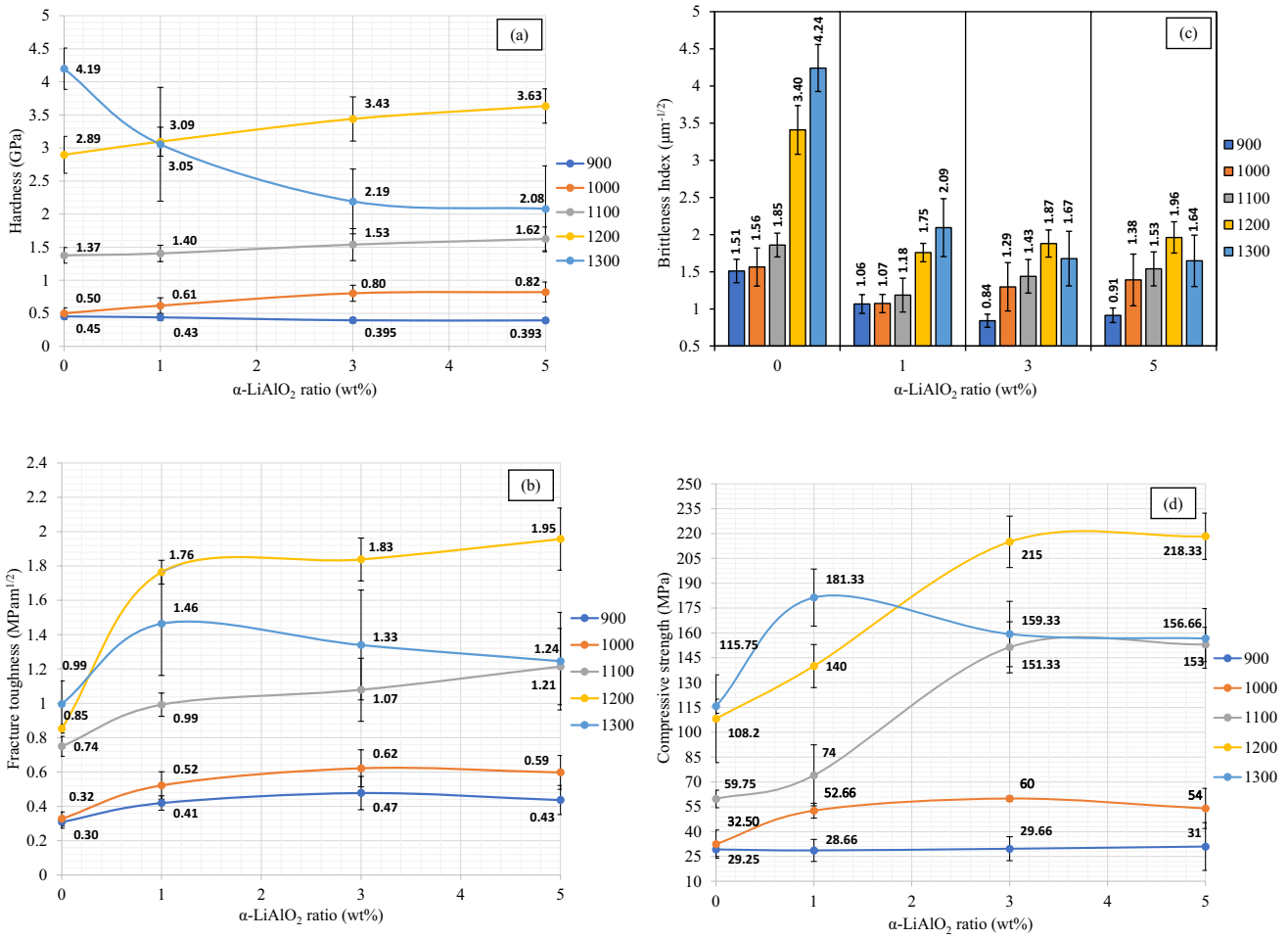


Fig. 8 Mechanical properties of pure BHA and α-$LiAlO_2$ incorporated BHAs

brittleness index decreased from 2.09 ± 0.38 to 1.64 ± 0.34 $\mu^{-1/2}$, and the compressive strength decreased from 181.33 ± 17.24 to 156.66 ± 16.02 MPa with increasing in the incorporation ratio of α-$LiAlO_2$. It was concluded that two main factors could be effective in the reduction of these characteristics. First is the more porosity content of these samples compared to pure BHA ($1.12 \pm 0.75\%$) and 1 wt% α-$LiAlO_2$ incorporated BHA ($0.83 \pm 0.18\%$). The porosity content of 3 and 5 wt% α-$LiAlO_2$ incorporated BHAs was $1.5 \pm 0.54\%$ and $4.59 \pm 0.19\%$ (Fig. 7d), respectively. Second is the presence of the residual hydroxyls and their association in pores at grain boundaries, which at a sufficiently high temperature exert the stress in the sample causing it to plastically deform, and hence the resultant microcracking [75]. Sintering helps to the densification and increasing the mechanical properties of HA ceramics. The results indicated that the relative density of BHA increased from 64.55 ± 0.69 to $90.77 \pm 1.51\%$, and the open porosity ratio decreased from 34.96 ± 0.56 to $1.12 \pm 0.75\%$, as the sintering temperature attained from 900 to 1300 °C. At this temperature, the density of 2.86 ± 0.04 g/cm^3, the hardness of 4.19 ± 0.31 GPa, the fracture toughness of 0.99 ± 0.13 MPam$^{1/2}$, and the compression strength of 115.75 ± 4.27 MPa were obtained for pure BHA. Relative density for α-$LiAlO_2$ incorporated BHAs increases with sintering temperature to reach its maximum value of $90.75 \pm 0.17\%$ at 1200 °C (Fig. 7c). The incorporation of α-$LiAlO_2$ contributed to increase in the density of BHA at a minimum of 2.30% and a maximum of 16.59% up to this temperature (Fig. 7b). It is thought that this can be due to three reasons: the first is that α-$LiAlO_2$ (1700 °C [76]) has a lower melting temperature than oxide ceramics added to BHA in previous studies such as TiO_2 (1843 °C [77]), Al_2O_3 (2070 °C [78]), ZrO_2 (2715 °C [79]), and MgO (2815 °C [80]). Second is the positive effect on increasing the sinterability of BHA. Third is the phases formed in α-$LiAlO_2$ incorporated BHAs (γ-$LiAlO_2$: 2.62 g/cm^3 [52], $CaAl_4O_7$: 2.91 g/cm^3, $Ca_4Al_6O_{13}$: 3.548 g/cm^3 [80], $Ca_9Al_6O_{18}$: 3.03 g/cm^3 [81]) have generally higher theoretical densities than that of pure BHA (β-TCP: 3.07 g/cm^3, α-TCP: 2.86 g/cm^3 [82]). Above that temperature, the

maximum relative density of 89.94 ± 0.12% was obtained to 1 wt% α-$LiAlO_2$ incorporated BHA, but it decreased to 85.85 ± 0.50%, being minimum with the incorporation of α-$LiAlO_2$ at amount 5 wt%. The decrease in relative density of 4.41% at 1300 °C is related to the presence of microcracks, exaggerated growth grains, and increase in the decomposition ratio of BHA to TTCP. Although the incorporation of α-$LiAlO_2$ to BHA caused to the formation of TTCP, the highest decomposition ratio obtained in this study was calculated as 1.2%. Therefore, a higher densification was obtained in the present study compared to SiO_2, MgO, Al_2O_3, and ZrO_2 incorporated BHAs at amount of 5 wt% [83], at the sintering temperature of 1300 °C. Hardness and fracture toughness of pure BHA increased by sintering temperature and reached to maximum values of 4.19 GPa and 0.99 ± 0.13 $MPam^{1/2}$ at 1300 °C, as shown in Fig. 8a and b, respectively. The fracture toughness values for most monolithic HA reported in the literature varied at 0.6–1 MPa $m^{1/2}$ [84]. Studies of the Vickers indentation hardness of HA indicate that hardness are largely influenced by the porosity and the presence of β-TCP [85]. It is well-known that hardness in sintered materials increase by decreasing porosity. Literature also reports that the β-TCP phase improves the hardness and fracture toughness of HA, if its amount in HA not to exceed 10% [86]. The highest hardness (3.63 ± 0.26 GPa) and fracture toughness (1.95 ± 0.18 $MPam^{1/2}$) for α-$LiAlO_2$ incorporated BHAs were obtained to the sample containing 5 wt% α-$LiAlO_2$, which was sintered at 1200 °C. This is attributed to the homogeneous microstructure and to the reduced free path for dislocations [87]. Although 1 wt% $LiAlO_2$ incorporated BHA contains less porosity than the other composites and its grain size is lower than BHA, the hardness of composites was lower than pure BHA, at 1300 °C. Moreover, the hardness of 1 wt% α-$LiAlO_2$ incorporated BHA at 1300 °C (3.05 ± 0.86 GPa) is reduced by 1.29% compared to the hardness at 1200 °C (3.09 ± 0.26 GPa). This may be related to the positive effect of 1 wt% α-$LiAlO_2$ on increasing the hardness of BHA is lower than that of 3, 5 wt% α-$LiAlO_2$ incorporations, as in all sintering temperatures except 900 °C. Despite the low hardness of α-$LiAlO_2$ incorporated BHAs at sintering of 1300 °C, the fracture toughness values (1 wt% α-$LiAlO_2$-BHA: 1.46 ± 0.30 $MPam^{1/2}$, 3 wt% α-$LiAlO_2$-BHA: 1.33 ± 0.31 $MPam^{1/2}$, 5 wt% α-$LiAlO_2$-BHA: 1.24 ± 0.28 $MPam^{1/2}$) are higher for this temperature compared to pure BHA (0.99 ± 0.13 $MPam^{1/2}$). This can be related to three reasons: first is the occurance of $\alpha \rightarrow \gamma$-$LiAlO_2$ transformation enable to promote crack deflection during microindentation testing. The same effect had also confirmed to the HA-ZrO_2 composites due to the occurance of tetragonal to the monoclinic (t-m) zirconia phase transformation [88]. Second is the calcium aluminates detected in the present study, which are thought to form in the interface regions of BHA and α-$LiAlO_2$ particulates have a positive effect increasing the fracture toughness, as in HA-Al_2O_3 composites [89]. Third is the microcracks caused by the formation of the TTCP phase, which is due to the decomposition of BHA, act as a barrier to the propagation of the cracks during the indentation test. Figure 8c shows the brittleness index of BHA with and without α-$LiAlO_2$ incorporations depending on the sintering temperature. The brittleness index is the parameter which indicates the lower resistance offered by a material surface towards crack propagation [90]. The brittle index displayed an increase with sintering temperature and reached to the maximum value of 4.24 ± 0.31 $\mu^{-1/2}$ for pure BHA. However, this value was found to be lower than a synthetic HA (9.39 $\mu^{-1/2}$) [91]). The brittleness index of the pure BHA is higher than the α-$LiAlO_2$ incorporated samples, at all sintering temperatures. The brittleness index of α-$LiAlO_2$ incorporated BHAs change between 0.84 ± 0.08 and 2.09 ± 0.38 $\mu^{-1/2}$. These values are considerably lower than MgO-doped synthetic HA (3.72 $\mu^{-1/2}$ [92]) and compatible with miserite glass ceramics (1.11 ± 0.05 $\mu^{-1/2}$ [93]), which was developed for use in dental applications. As shown in Fig. 8d, the highest compressive strength for pure BHA was obtained as 115.75 ± 4.27 MPa. This value is in agreement with previous studies [94, 95]. At the same temperature, the compressive strength of BHA increased by 56%, and a compressive strength of 181.33 MPa was obtained in 1 wt% α-$LiAlO_2$ incorporated sample. This ratio was calculated as 85.74% (215 ± 15.50 MPa for 3 wt% α-$LiAlO_2$ composite) and 88.62% (218 ± 14.02 MPa for 3 wt% α-$LiAlO_2$ composite) at 1200 °C. In these composite, the compressive strength decreased to 159.33 ± 19.69 MPa and 156.66 ± 18.02 MPa, respectively. The same regime had also confirmed by ref [96]. This is related to two main reasons: first is the decomposition of HA to TTCP can prevent the formation of strong inter-particle bonding in the ceramic [97]. Second is the high porosity in these samples. Pores give a negative effect on strength by two ways: they act as stress raiser, meaning that the stress concentration is high at these pores. If this stress together with the applied stress surpasses a certain limit, a crack will develop. The crack will propagate spontaneously and the material will fail. Pores also reduce the cross-sectional area at which the load is applied [98].

The bioactivity of ceramics has been defined as "the bond ability with host bone tissue." The SBF method is a useful way to test the in vitro bioactivity of bioceramics for the assessment of the apatite formation potential [99]. Figure 9 shows the surface morphologies of pure BHA and 5 wt% α-$LiAlO_2$ incorporated BHA which have the highest mechanical properties, at the immersion times of 7, 14, and 28 days, respectively. A large number of apatite crystals formed in cubic form on the surface of pure BHA, after 7 days of immersion. The intensity of cubic apatite structures on the surface of BHA remerkably increased after

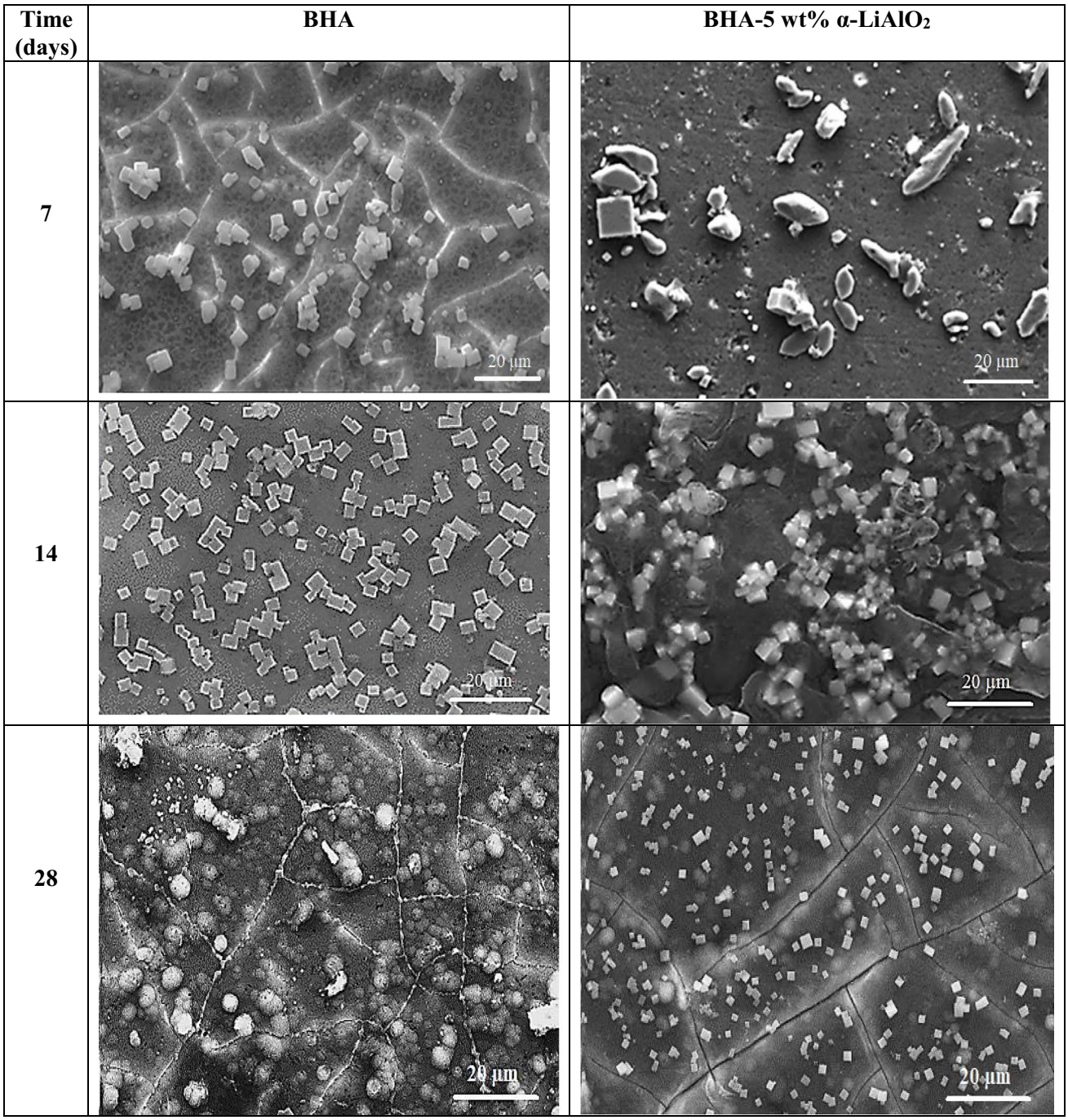


Fig. 9 SEM images of the apatite layers on the surface of pure BHA and 5 wt% α-$LiAlO_2$ incorporated BHA after immersing into the SBF solution

14 days of SBF testing. After 30 days of immersion, the surface of pure BHA was covered with highly dense apatite. This means that the apatite formation on the surface of pure BHA was increased with the increasing of SBF immersion days, which is consistent with a previous investigation [100]. The crack-like regions on the surface of samples that formed along the interfaces of the apatite layers are drying cracks [101]. The apatite structure on the surface of 5 wt% α-$LiAlO_2$ incorporated BHA is both less dense than pure BHA and is in flaky and/or rod-shaped instead of the cubic form observed on the surface of pure BHA at the end of immersing time of 7 days. The same apatite structures had also observed on the surface of carbon nanotube reinforced HA [102]. After 14 days of SBF testing, it was observed that

there was an increase in the number as well as change in the morphology (from flaky and/or rod to cubic) of the apatite structure on the surface of 5 wt% α-$LiAlO_2$ incorporated BHA. This indicates that the bioactivation for this material became clearly visible at 14 days. The apatite on the surface of 5 wt% α-$LiAlO_2$ incorporated BHA at 14 days was also thicker than that of 5 wt% Al_2O_3 incorporated HA. [103]. After 30 days of immersion, the surface of 5 wt% α-$LiAlO_2$ incorporated BHA was covered with highly dense apatite as in pure BHA. Densification at around 90% is also desirable because the presence of a certain degree of porosity, as well as of the reabsorbable (β- and/or α-TCP) and/or biocompatible phases contribute to bone inter-growth and a subsequent implant-bone interfacial adhesion [104]. The results show that the incorporation of 5 wt% α-$LiAlO_2$ into BHA contributes to increasing the sinterability and properties of BHA without decreasing its bioactivity.

Conclusions

In the present study, the effects of α-$LiAlO_2$ incorporation on the of BHA were evaluated by XRD and SEM as well as by the measurements of density, relative density, porosity, shrinkage, hardness, fracture toughness, brittleness index, and compressive strength. The following results were obtained:

- The properties of BHA are improved with the increase in sintering temperature. A shrinkage of $12.02 \pm 0.52\%$, density of 2.86 ± 0.47 g/cm^3, relative density of $90.77 \pm 1.51\%$, porosity of $1.12 \pm 0.75\%$, hardness of 4.19 GPa ± 0.31, fracture toughness of 0.99 ± 0.13 MPam$^{1/2}$, brittleness index of 4.24 ± 0.31 $\mu^{-1/2}$, and compressive strength of 115.75 ± 4.27 MPa were obtained to BHA without α-$LiAlO_2$ incorporation, when it was sintered at 1300 °C.
- Pure BHA started to decompose at 1100 °C and the decomposition rate was determined as 4.7% at 1300 °C.
- In composites, the highest properties were obtained for the 5 wt% α-$LiAlO_2$ incorporated BHA, when sintering was carried out at 1200 °C. For this composite, the density of 2.87 ± 0.00 g/cm^3, fracture toughness of 1.95 ± 0.18 MPam$^{1/2}$, compressive strength of 218.33 ± 14.02 MPa, and brittleness index of 1.96 ± 0.21 $\mu^{-1/2}$ were obtained.
- Sintering at 1300 °C led to decreasing in the properties of α-$LiAlO_2$ incorporated BHAs due to the decomposition, grain growth, and increase in porosity.
- In vitro bioactivity test shows that the bioactivation for 5 wt% α-$LiAlO_2$ incorporated BHA became clearly visible in 14 days.
- The results show that the incorporation of 5 wt% α-$LiAlO_2$ into BHA contributes to increasing the sinterability and properties of BHA without decreasing its bioactivity. However, it is recommended for use in applications such as tooth root replacements, filling periodontal pockets, cystic cavities, areas adjacent to implants, spinal fusions, contour and malformation defects and nonunions of long bones, due to its fracture toughness of less than 2–12 MPam$^{1/2}$.

Funding The author thanks the economic support of the Scientific Research Centre of Marmara University (Project No: FEN-A-110618–0335).

Declarations

Conflict of Interest The authors declare no competing interests.

References

1. Niakan, A., Ramesh, S., Naveen, S.V., Mohan, S., Kamarul, T.: Osteogenic priming potential of bovine hydroxyapatite sintered at different temperatures for tissue engineering applications. Mater. Lett. **197**, 83–86 (2017)
2. Ramesh, S., Loo, Z.Z., Tan, C.Y., Kelvin-Chew, W.J., Ching, Y.C., Tarlochan, F., Chandran, H., Krishnasamy, S., Bang, L.T., Sarhan, A.A.D.: Characterization of biogenic hydroxyapatite derived from animal bones for biomedical applications. Ceram. Int. **44**, 10525–10530 (2018)
3. Herliansyah, M.K., Hamdi, M., Ide-Ektessabi, A., Wildan, M.W., Toque, J.A.: The influence of sintering temperature on the properties of compacted bovine hydroxyapatite. Mater. Sci. Eng. C **29**, 1674–1680 (2009)
4. Pazarlioglu, S.S., Gokce, H., Ozyegin, S., Salman, S.: Effect of sintering on the microstructural and mechanical properties of meleagris gallopova hydroxyapatite. Biomed. Mater. Eng. **24**, 1751–1769 (2014)
5. Janus, A.M., Faryna, M., Haberko, K., Rakowska, A., Panz, T.: Chemical and microstructural characterization of natural hydroxyapatite derived from pig bones. Microchim Acta **161**, 349–353 (2008)
6. Foroutan, R., Peighambardoust, S.J., Hosseini, S.S., Akbari, A., Ramavandi, B.: Hydroxyapatite biomaterial production from chicken (femur and beak) and fish bone waste through a chemical less method for Cd^{2+} removal from ship building waste water. J Hazard Mater **413**, 125428 (2021)
7. Barakat, N.A.M., Khalil, K.A., Sheikh, F.A., Omran, A.M., Gaihre, B., Khil, S.M., Kim, H.Y.: Physiochemical characterizations of hydroxyapatite extracted from bovine bones by three different methods: extraction of biologically desirable HAp. Mater Sci Eng C **28**, 1381–1387 (2008)
8. Khoo, W., Nor, F.M., Ardhyananta, H., Kurniawan, D.: Preparation of natural hydroxyapatite from bovine femur bones using calcination at various temperatures. Procedia Manuf **2**, 196–201 (2015)
9. Kusrini, E., Sontang, M.: Characterization of x-ray diffraction and electron spin resonance: effects of sintering time and

temperature on bovine hydroxyapatite. Radiat Phys Chem **81**, 118–125 (2012)
10. Pazarlioglu, S., Algan, O., Isikogullari, A.M., Gokce, H.: The effect of lanthanum addition on the microstructure and mechanical properties of Mg-modified hydroxyapatite ceramics. Process Appl Ceram **15**(3), 226–237 (2021)
11. Salman, S., Gunduz, O., Yilmaz, S., Öveçoğlu, M.L., Snyder, R.L., Agathopoulos, S., Oktar, F.N.: Sintering effect on mechanical properties of composites of natural hydroxyapatites and titanium. Ceram Int **35**, 2965–2971 (2009)
12. Comín, R., Cid, M.P., Grinschpun, L., Oldani, C., Salvatierra, N.A.: Titanium-hydroxyapatite composites sintered at low temperature for tissue engineering: in vitro cell support and biocompatibility. J Appl Biomater Funct Mater **15**(2), 176–183 (2017)
13. Kim, Y.G., Seo, D.S., Lee, J.K.: Dissolution of synthetic and bovine bone-derived hydroxyapatites fabricated by hot-pressing. Appl Surf Sci **255**, 589–592 (2008)
14. Maidaniuc, A., Miculescu, F., Mocanu, A.C., Voicu, ŞI., Miculescu, M., Purcaru, A., Muhuleţ, A., Pop, C., Rada, M.E.: Sinterability study of bovine-derived hydroxyapatite and silver microcomposites. UPB Sci Bull Series B **79**(1), 145–154 (2017)
15. Szewczyk-Nykiel, A., Nykiel, M.: Analysis of the sintering process of 316L-hydroxyapatite composite biomaterials. Tech Trans Mech **3–M**, 79–92 (2015)
16. Dorozhkin, S.V.: Bioceramics of calcium orthophosphates. Biomaterials **31**, 1465–1485 (2010)
17. Willmann, G.: Coating of implants with hydroxyapatite-material connections between bone and metal. Adv Eng Mater **1**, 95–105 (1999)
18. Gunduz, O., Gode, C., Ahmad, Z., Gökçe, H., Yetmez, M., Kalkandelen, C., Sahin, Y.M., Oktar, F.N.: Preparation and evaluation of cerium oxide-bovine hydroxyapatite composites for biomedical engineering applications. J Mech Behav Biomed Mater **35**, 70–76 (2014)
19. Öksüz, K.E., Özer, A.: Effect of yttria on the phase formation and sintering of HA-Al_2O_3 biocomposites. Acta Phys Pol **131**(3), 576–579 (2017)
20. Gunduz, O., Ozyegin, L.S., Dorozhkin, S., Meydanoglu, O., Eruslu, N., Kayali, S., Agathopoulos, S., Oktar, F.N.: Bovine hydroxyapatite (BHA) boron oxide composites. Key Eng Mater **396–398**, 403–406 (2009)
21. Gunduz, O., Ozyegin, L.S., Dorozhkin, S., Meydanoglu, O., Eruslu, N., Kayali, S., Goller, G., Agathopoulos, S., Oktar, F.N.: Bovine hydroxyapatite (BHA) strontium oxide composites. Key Eng Mater **396–398**, 407–410 (2009)
22. Gunduz, O., Erkan, E.M., Daglilar, S., Salman, S., Agathopoulos, S., Oktar, F.N.: Composites of bovine hydroxyapatite (BHA) and ZnO. J. Mater Sci **43**, 2536–2540 (2008)
23. Oktar, F.N.: Hydroxyapatite-TiO_2 composites. Mater Lett **60**, 2207–2210 (2006)
24. Unal, S., Ekren, N., Sengil, A.Z., Oktar, F.N., Irmak, S., Oral, O., Sahin, Y.M., Kilic, O., Agathopoulos, S., Gunduz, O.: Synthesis characterization and biological properties of composites of hydroxyapatite and hexagonal boron nitride. J Biomed Mater Res Part B Appl Biomater **106**(6), 2384–2392 (2018)
25. Yetmez, M., Erkmen, Z.E., Kalkandelen, C., Ficai, A., Oktar, F.N.: Sintering effects of mullite-doping on mechanical properties of bovine hydroxyapatite. Mater Sci Eng C **77**, 470–475 (2017)
26. Celik, H.H., Gunduz, O., Ekren, N., Ahmad, Z., Oktar, F.N.: Predicting the mechanical properties of BHA-Li_2O composites using artificial neural networks. J Biomater Nanobiotechnol **2**, 98–101 (2011)
27. Shainberg, A.P.M., Valério, P., Zonari, A., Oktar, F.N., Ozyegin, L.S., Grac, M.P.F., Leite, M.F., Goes, A.M.: Attachment and proliferation of osteoblasts on lithium-hydroxyapatite composites. Adv Mater Sci Eng (2012). https://doi.org/10.1155/2012/650574
28. Du, J., Poelman, D.: Energy efficient microwave-assisted preparation of deep red/near-infrared emitting lithium aluminate and gallate phosphors. J. of Lumin. **237**, 118168 (2021)
29. Suriyamurthy, N., Panigrahi, B.S., Natarajan, A.: Luminescence study of iron doped lithium aluminate phosphors. Mater Sci Eng A **403**, 182–185 (2005)
30. Marezio, M., Remeika, J.P.: High-pressure synthesis and crystal structure of α-$LiAlO_2$. J Chem Phys **44**(8), 3143–3144 (1966)
31. Fischer, A. K.: Atmospheric pressure synthesis for β-$LiAlO_2$. Inorg Chem 16(4), 974–974 (1977), Marezio, M. The crystal structure and anomalous dispersion of γ-$LiAlO_2$. Acta Crystallograp 19(**3**), 396–400 (1965)
32. Twardak, A., Bilski, P., Marczewska, B., Gieszczyk, W.: Analysis of TL and OSL kinetics of lithium aluminate. Radiat Meas **71**, 143–147 (2014)
33. Gao, J., Shi, S., Xiao, R., Li, H.: Synthesis and ionic transport mechanisms of α-$LiAlO_2$. Solid State Ion **286**, 122–134 (2016)
34. Thi, N., Ha, T., Giap, T.V., Thanh, N.T.: Synthesis of lithium aluminate for application in radiation dosimetry. Mater Lett **267**, 127506 (2020)
35. Wani, M.A., Dhoble, S.J., Belekar, R.M.: Synthesis, characterization and spectroscopic properties of some rare earth activated $LiAlO_2$ phosphor. Optik **226**, 165938 (2021)
36. Pazarlioglu, S., Salman, S.: Sintering effect on the microstructural, mechanical, and in vitro bioactivity properties of a commercially synthetic hydroxyapatite. J Aust Ceram Soc **53**, 391–401 (2017)
37. Ruys, A.J., Wei, M., Sorrell, C.C., Dickson, M.R., Brandwood, A., Milthorpe, B.K.: Sintering effects on the strength hydroxyapatite. Biomaterials **16**, 409–415 (1995)
38. Beckerman, S., Ford, R., Nemeth, M.: Conversion of gamma lithium aluminate to lithium aluminum carbonate hydroxide hydrate. Powder Diffr **11**(4), 312–317 (1996)
39. Pandey, A., Nigam, V.K., Balani, K.: Multi-length scale tribology of hydroxyapatite reinforced with ceria and silver. Wear **404–405**, 12–21 (2018)
40. Kokubo, T., Yamamuro, T., Hench, L.L., Wilson, J.: Handbook on bioactive ceramics: bioactive glasses and glass-ceramics. Boca Raton (1990)
41. Ooi, C.Y., Hamdi, M., Ramesh, S.: Properties of hydroxyapatite produced by annealing of bovine bone. Ceram Int **33**, 1171–1177 (2007)
42. Brzezínska-Miecznik, J., Haberko, K., Búcko, M.M., Grabowski, G., Sitarz, M.: Hydroxyapatite of natural origin-zirconia composites, preparation and reactions within the system. Process Appl Ceram **10**(4), 219–225 (2016)
43. The British Standards Institution 2018, ISBN 978 0 580 86939–6
44. Barros, B.S., de Oliveira, R.S., Kulesza, J., Melo, V.R.M., Melo, D.M.A., Alves, S.: $Ca_{3-x}Al_2O_6$:xEu^{3+} nanophosphors: fast synthesis and photophysical properties. J Phys Chem Solids **78**, 90–94 (2015)
45. Chen, X., Yang, L., Zhou, Z., Chengi, Z.: Core-shell structured CaO-$Ca_9Al_6O_{18}$@$Ca_5Al_6O_{14}$/Ni bifunctional material for sorption-enhanced steam methane reforming. Chem Eng Sci **163**, 114–122 (2017)
46. López, F.A., Martín, M.I., Alguacil, F.J., Ramírez, M.S., González, J.R.: Synthesis of calcium aluminates from non-saline aluminum dross. Mater **12**, 1837–1849 (2019)
47. Konar, B., Jung, I.H.: A coupled phase diagram experimental study and thermodynamic optimization of the Li_2O-CaO-Al_2O_3 and Li_2O-CaO-SiO_2 systems, and prediction of the phase diagrams of the Li_2O-CaO-Al_2O_3-SiO_2 system. J Eur Ceram Soc **40**, 2185–2199 (2020)

48. Evis, Z., Doremus, R.H.: Effect of AlF_3, CaF_2 and MgF_2 on hot-pressed hydroxyapatite-nanophase alpha-alumina composites. Mater Res Bull **43**, 2643–2651 (2008)
49. Yuan, X., Xu, Y., He, Y.: Synthesis of $CaAl_4O_7$ via citric acid precursor. J. Alloys Compd. **441**, 251–254 (2007)
50. Palchesko, R.N., McGowan, K.A., Gawalt, E.S.: Surface immobilization of active vancomycin on calcium aluminum oxide. Mater Sci Eng C **31**, 637–642 (2011)
51. Yuan, X., Xu, Y.B., He, Y.: Synthesis of $Ca_3Al_2O_6$ via citric acid precursor. Mater Sci Eng A **447**, 142–145 (2007)
52. Kahlenberg, V., Fischer, R.X., Shaw, C.S.J.: High-pressure $Ca_4Al_6O_{13}$: an example of a calcium aluminate with three different types of coordination polyhedra for aluminum. Am Mineral **85**, 1492–1496 (2000)
53. Danek, V., Tarniowy, M., Suski, L.: Kinetics of the $\alpha \rightarrow \gamma$ phase transformation in $LiAlO_2$ under various atmospheres within the 1073–1173 K temperatures range. J Mater Sci **39**, 2429–2435 (2004)
54. Li, X., Wang, X., Hu, R., Li, Y., Yao, X.: Modulating trap levels via co-doping Ca^{2+}/Si^{4+} in $LiTaO_3:Pr^{3+}$ to improve both the intensity and threshold of mechanoluminescence. J Alloys Compd **896**, 1628772 (2021)
55. Jerebtsov, D.A., Mikhailov, G.G.: Phase diagram of $CaO\text{-}Al_2O_3$ system. Ceram Int **27**, 25–28 (2001)
56. Moseke, C., Gbureck, U.: Tetracalcium phosphate: synthesis, properties and biomedical applications. Acta Biomater **6**, 3815–3823 (2010)
57. Nizara, M.S., Sofiyaningsih, N., Manullang, R.J., Wijayanti, R.B., Rosmayanti, I., Sumardan, D.: Novel fast firing method to synthesize tetracalcium phosphate. AIP Conf Proc (2021). https://doi.org/10.1063/5.0051750
58. Behnamghader, A., Bagheri, N., Raissi, B., Moztarzadeh, F.: Phase development and sintering behaviour of biphasic HA-TCP calcium phosphate materials prepared from hydroxyapatite and bioactive glass. J. Mater Sci: Mater Med **19**, 197–201 (2008)
59. Ozturk, S., Yetmez, M.: Studies on characterization of bovine hydroxyapatite/$CaTiO_3$ biocomposites. Adv Mater Sci Eng (2016). https://doi.org/10.1155/2016/6987218
60. Pazarlioglu, S.S., Salman, S.: The effect of alumina additive and sintering temperature on the microstructural, physical, mechanical, and bioactivity properties of hydroxyapatite-alumina composites. J Aust Ceram Soc **56**, 413–431 (2020)
61. Rincón-López, J.A., Hermann-Muñoz, J.A., Fernández-Benavides, D.A., Giraldo-Betancur, A.L., Alvarado-Orozco, J.M., Muñoz-Saldaña, J.: Isothermal phase transformations of bovine-derived hydroxyapatite/bioactive glass: a study by design of experiments. J Eur Ceram Soc **39**, 1613–1624 (2019)
62. Göller, G., Oktar, F.N.: Sintering effects on mechanical properties of biologically derived dentine hydroxyapatite. Materi Lett **56**, 142–147 (2002)
63. Miao, X., Chen, Y., Guo, H., Khor, K.A.: Spark plasma sintered hydroxyapatite-yttria stabilized zirconia composites. Ceram Int **30**, 1793–1796 (2004)
64. Pazarlioglu, S.: Hydroxyapatite/cerium oxide composites: sintering, microstructural, mechanical and in-vitro bioactivity properties. Int. J Adv Eng Pure Sci **4**, 295–304 (2019)
65. Halouanı, R., Bernache-Assolant, D., Champion, E., Ababou, A.: Microstructure and related mechanical properties of hot pressed hydroxyapatite ceramics. J Mater Sci: Mater Med **5**, 563–568 (1994)
66. Hoepfner, T.P., Case, E.D.: An estimate of the critical grain size for microcracks induced in hydroxyapatite by thermal expansion anisotropy. Mater Lett **58**, 489–492 (2004)
67. Es-saddik, M., Laasri, S., Taha, M., Laghzizil, A., Guidara, A., Chaari, K., Bouaziz, J., Hajjaji, A., Nunzi, J.M.: Effect of the surface chemistry on the stability and mechanical properties of the Zirconia-Hydroxyapatite bioceramic. Surf Interfaces **23**, 100980 (2021)
68. Wang, C.K., Ju, C.P., Chem Lin, J.H.: Effect of doped bioactive glass on structure and properties of sintered hydroxyapatite. Mater Chem Phys **53**, 138–149 (1998)
69. Kantana, W., Jarupoom, P., Pengpat, K., Eitssayeam, S., Tunkasiri, T., Rujijanagul, G.: Properties of hydroxyapatite/zirconium oxide nanocomposites. Ceram Int **39**, 379–382 (2013)
70. Farzin, A., Ahmadian, M., Fathi, M.H.: Comparative evaluation of biocompatibility of dense nanostructured and microstructured Hydroxyapatite/Titania composites. Mater Sci Eng C **33**, 2251–2257 (2013)
71. Mobasherpour, I., Salahi, E.: Effect of heat treatment on grain growth of nanocrystalline hydroxyapatite powder. J Ceram Sci Tech **02**(02), 119–124 (2011)
72. Xuebin, Z., Yunfei, D., Songlin, W., Jie, X., Yi, F.: Sintering behavior and kinetic evaluation of hydroxyapatite bio-ceramics from bovine bone. Ceram. **54**(3), 248–252 (2010)
73. Sych, O., Pinchuk, N., Ivanchenko, L.: Structure evolution and properties of biogenic hydroxyapatite-based biocomposite. Process App Ceram **3**(3), 157–160 (2009)
74. Majling, J., Zńaik, P., Palová, A., Svetík, S.: Sintering of the ultrahigh pressure densified hydroxyapatite monolithic xerogels. J Mater Res **12**(1), 198–202 (1997)
75. Tabero, P., Frąckowiak, A., Dąbrowska, G.: Reinvestigations of the $Li_2O\text{-}Al_2O_3$ system Part I: $LiAlO_2$ and Li_3AlO_3. Pol J Chem Technol **23**(3), 30–36 (2021)
76. Mahdi, M.T., Kara, I.H.: Thermophysical characteristic of nano-TiO_2 paraffin wax composite material. J Mech Eng Res Dev **44**(6), 48–58 (2021)
77. Schneider, S.J., McDaniel, C.L.: Effect of environment upon the melting point of Al_2O_3. J Res Nat Bureau Stand A Phys Chem **71**(4), 317–333 (1967)
78. Kondo, T., Muta, H., Kurosaki, K., Kargl, F., Yamaji, A., Furuya, M., Ohishi, Y.: Density and viscosity of liquid ZrO_2 measured by aerodynamic levitation technique. Heliyon **5**, e02049 (2019)
79. Ronchi, C., Sheindlin, M.: Melting point of MgO. J Appl Phys **90**, 3325–3331 (2001)
80 Li, T.K., Dickon, H.L., Ng: Formation of γ-$LiAlO_2$ nano-network in an Al-based metal matrix composite. Mater Lett **61**, 1109–1113 (2007)
81. Jeffery, J.W., Mondal, P.: Zeitschriftfuer Kristallographie, Kristallgeometrie, Kristallphysik, Kristallchemie (-144 1977), **73**, 17 (1929)
82. Sallemi, I., Bouaziz, J., Ayed, F.B.: Elaboration and characterization of bioceramic based on tricalcium phosphate and zirconia. Int J Curr Eng Technol **3**(5), 1691–1700 (2013)
83. Oktar, F.N., Agathopoulos, S., Ozyegin, L.S., Gunduz, O., Demirkol, N., Bozkurt, Y., Salman, S.: Mechanical properties of bovine hydroxyapatite (BHA) composites doped with SiO_2, MgO, Al_2O_3, and ZrO_2. J Mater Sci: Mater Med **18**, 2137–2143 (2007)
84. Ramesh, S., Jeffrey, C.K.L., Tan, C.Y., Wong, Y.H., Ganesan, P., Ramesh, S., Kutty, M.G., Chandran, H., Devaraj, P.: Sintering behaviour and properties of magnesium orthosilicate hydroxyapatite ceramic. Ceram Int **42**, 15756–15761 (2016)
85. Hoepfner, T.P., Case, E.D.: The influence of the microstructure on the hardness of sintered hydroxyapatite. Ceram Int **29**, 699–706 (2003)
86. Lopes, M.A., Monteiro, F.J., Jose, H., Santos, D.: Glass-reinforced hydroxyapatite composites: fracture toughness and hardness dependence on microstructural characteristics. Biomaterials **20**, 2085–2090 (1999)
87. Wang, J., Shaw, L.L.: Nanocrystalline hydroxyapatite with simultaneous enhancements in hardness and toughness. Biomaterials **30**, 6565–6572 (2009)

88. Fakhraei, O., Hesaraki, S., Alizadeh, M.: Fracture toughness and R-curve behavior of BCP/YTZP nanocomposites produced using the spark plasma sintering process. J Alloys Compd **725**, 623–631 (2017)
89. Evis, Z., Doremus, R.H.: A study of phase stability and mechanical properties of hydroxylapatite-nanosize α-alumina composites. Mater Sci Eng C **27**, 421–442 (2007)
90. Pal, A., Metya, A.K., Chowdhury, A.R., Sinha, A.: Structural and mechanical behavior of mechanochemically synthesized nanocrystalline hydroxyapatite from mercenaria clam shells. Trans Ind Ceram Soc **79**(4), 175–181 (2020)
91. Bianco, A., Cacciotti, I., Lombardi, M., Montanaro, L., Bemporad, E., Sebastiani, M.: F-substituted hydroxyapatite nanopowders: thermal stability, sintering behaviour and mechanical properties. Ceram Int **36**, 313–322 (2010)
92. Shaly, A.A., Priya, G.H., Linet, J.M.: An exploration on the configurational and mechanical aspects of hydrothermally procured MgO/HA bioceramic nanocomposite. Phys B **617**, 413131 (2021)
93. Saadaldin, S.A., Dixon, S.J., Costa, D.O., Rizkalla, A.S.: Synthesis of bioactive and machinable miserite glass-ceramics for dental implant applications. Dent Mater **29**, 645–655 (2013)
94. Altintas, S., Gokbayrak, H., Goren, S.: Production of hydroxyapatite from animal bone. Key Eng Mater **264–268**, 1949–1952 (2004)
95. Goller, G., Oktar, F.N., Agathopoulos, S., Tulyaganov, D.U., Ferreira, J.M.F., Kayali, E.S., Peker, I.: Sintering effects of temperature on mechanical and microstructural properties of bovine hydroxyapatite (BHA). J Sol-Gel Sci Tech **37**, 111–112 (2006)
96. Bozkurt, Y., Pazarlioglu, S., Gokce, H., Gurler, I., Salman, S.: Hydroxyapatite lanthanum oxide composites. Acta Phys Pol A **127**, 1407–1409 (2015)
97. Dou, J., Zhang, C., Chen, C., Zhang, X.: Effects of sintering temperature on the properties of alumina/ hydroxyapatite composites. J Sol-Gel Sci Technol **84**, 23–27 (2017)
98. Nawang, R., Hussein, M.Z., Matoria, K.A., Abdullah, C.A.C., Hashim, M.: Physicochemical properties of hydroxyapatite/ montmorillonite nanocomposite prepared by powder sintering. Results Phys **15**, 102540 (2019)
99. Wu, C., Xiao, Y.: Evaluation of the in vitro bioactivity of bioceramics. Bone Tissue Regener Insights **2**, 25–29 (2009)
100. Horkavcová, D., Rohanová, D., Kuncová, L., Zítková, K., Cílová, Z.Z., Helebrant, A.: Comparison of reactivity of synthetic and bovine hydroxyapatite in vitro under dynamic conditions. Ceram **58**(1), 70–78 (2014)
101. Lin, C., Lin, J.H., Ding, H.J., Ju, C.P.: Characterization of immersed hydroxyapatite-bioactive glass coatings in Hank's solution. Mater Chem Phys **64**, 229–240 (2000)
102. Zhao, S., Cui, W., Rajendran, N.K., Su, F., Rajan, M.: Investigations of gold nanoparticles-mediated carbon nanotube reinforced hydroxyapatite composite for bone regenerations. J Saudi Chem Soc **25**, 101261 (2021)
103. Pazarlioglu, S., Salman, S.: Effect of yttria on thermal stability, mechanical and in vitro bioactivity properties of hydroxyapatite/ alumina composite. J Ceram Process Res **20**(1), 99–112 (2019)
104. Silva, V.V., Lameiras, F.S., Domingues, R.Z.: Microstructural and mechanical study of zirconia-hydroxyapatite (ZH) composite ceramics for biomedical applications. Compos Sci Technol **61**, 301–310 (2001)

Publisher's note Springer Nature remains neutral with regard to jurisdictional claims in published maps and institutional affiliations.

Springer Nature or its licensor holds exclusive rights to this article under a publishing agreement with the author(s) or other rightsholder(s); author self-archiving of the accepted manuscript version of this article is solely governed by the terms of such publishing agreement and applicable law.